IEEE Access
Multidisciplinary ⋮ Rapid Review ⋮ Open Access Journal

Received June 24, 2019, accepted July 8, 2019, date of publication July 12, 2019, date of current version July 29, 2019.

Digital Object Identifier 10.1109/ACCESS.2019.2928380

Precise Geometric Correction and Robust Mosaicking for Airborne Lightweight Optical Butting Infrared Imaging System

FANLU WU[1], HAINAN GUAN[1], DEJIE YAN[1], ZHENG WANG[1], DONG WANG[1], AND QINGYU MENG[1,2]

[1]Changchun Institute of Optics, Fine Mechanics and Physics, Chinese Academy of Sciences, Changchun 130033, China
[2]Research Center for Space Optical Engineering, Harbin Institute of Technology, Harbin 150001, China

Corresponding author: Qingyu Meng (mengqy@ciomp.ac.cn)

This work was supported in part by the National Natural Science Foundation of China under Grant 61705220 and Grant 61805001, in part by the Youth Innovation Promotion Association, Chinese Academy of Sciences, under Grant 2019219, in part by the ShuGuang Talents Scheme Award of Changchun Institute of Optics, Fine Mechanics and Physics, Chinese Academy of Sciences, and in part by the Strategic Priority Research Program of Chinese Academy of Sciences under Grant XDA17010205.

ABSTRACT In view of the urgent need for high-resolution and high-precision infrared image data for geological environmental monitoring, we have developed a lightweight optical butting infrared imaging system for unmanned aerial vehicles (UAVs) to obtain infrared image data. In this paper, we proposed a robust mosaicking method combination of as-projective-as-possible warps and similarity transformation, which uses multiple images to generate a wide viewing field panorama. It is developed based on an analysis of projective transformation and similarity transformation. The proposed method simultaneously takes into consideration the flexibility of alignment and the preservation of image shapes. On the overlapping regions, it performs as-projective-as-possible warps. On the non-overlapping regions, it gradually becomes a similarity warp. The results show that the proposed method weakens the ''ghosting,'' shape distortion, and area distortion.

INDEX TERMS Image mosaicking, non-linear distortion correction, trapezoidal distortion correction, UAVs.

I. INTRODUCTION

In view of the urgent need for high-resolution and high-precision infrared image data for geological environmental monitoring (geological hazards, groundwater and mine resources), multi-rotor UAVs (Unmanned Aerial Vehicles) [1]–[4] airborne infrared imaging system has become a practical solution. In recent years, UAVs photoelectric imaging system has attracted wide attention with its advantages of high real-time and flexibility. Especially, low-altitude flight of small and medium-sized multi-rotor UAVs can achieve high-resolution imaging with low cost, low risk and short development cycle. It has been widely used in vegetation forest research [5], fine agriculture [6], three-dimensional reconstruction [7], field search and rescue [8], disaster investigation [9] and other civil fields.

A single image from a UAV mounted camera only covers a limited area. In many applications, it is necessary to stitch hundreds or even thousands of images together to create a panorama that can provide good overall situational awareness [10]–[12]. In the past two decades, image mosaicking [13]–[16] has been applied in solving practical problems in different fields, such as deep space exploration [17]–[20], virtual reality [21], motion analysis [22], satellite remote sensing image processing [23]–[25] and so on. The image mosaicking algorithms represented by AutoStitch[1] [26] and Microsoft's ICE (Image Compositing Editor[2]) are quite mature. These algorithms require that the input image must satisfy the following assumptions: the actual scene corresponding to the overlapping area can ignore the change in depth direction. If this assumption is not satisfied, there

The associate editor coordinating the review of this manuscript and approving it for publication was Lefei Zhang.

[1]http://matthewalunbrown.com/autostitch/autostitch.html
[2]https://www.microsoft.com/en-us/research/product/computational-photography-applications/image-composite-editor/

will be yielding misalignment artifacts or ''ghosting'' in the results due to the parallax problem. Existing techniques use a single global homography per image to perform the alignment. Obviously, a single global homography matrix cannot solve the parallax problem. Gao *et al*. [27] demonstrated how to use DHW (Dual-Homography Warping) to align images of panoramic scenes containing a dominant distant and ground plane. The algorithm has a good effect on the scene mosaic, which can be clearly divided into two predominate planes: a distant back plane and a ground plane. But it is difficult to extend to any scene to achieve seamless mosaic, and requires manual intervention and post-processing. Zaragoza *et al*. [28] proposes APAP (As-Projective-As-Possible) warps for image stitching, divides the frame into many cells, and calculates the projective transformation model for each cell using SIFT (Scale Invariant Feature Transform) features [29], [30]. Depending on these projective transformation models, each cell is aligned with the reference frame based on a local warping process. The multi-cell alignment strategy partially solves the problem that the different projections exist in the different image regions. However, the transformation used in the non-overlapping region of the algorithm is approximately in the global projection transformation, so this part of the image will have distortion problems, especially the stretching phenomenon of the field of view edge is serious. The mosaicking performance is mainly determined by the feature matching results [31]–[34]. A popular strategy for solving the matching problem involves two steps: first computing a set of putative correspondences, and then removing the outliers via geometrical constraints [35]–[37].

Airborne imaging system cannot obtain an ideal image. In addition to lens distortion, the errors introduced by mechanical working and adjusting will also make the image produce different degrees of non-linear distortion [38]. Therefore, it is necessary to correct the non-linear distortion of the obtained original image. Lens distortion is usually classified into three types: radial distortion, decentering distortion, and thin prism distortion. In practice, for most lenses, the radial distortion component is predominant [39]. Methods used for obtaining the parameters in the radial distortion function for correcting the distorted images can be divided roughly into two major categories: multiple views method [40]–[42] and single view method [43]–[45]. In [39], a method based on the use of distorted straight lines falls in the second category. The method works on a single image in which at least three distorted straight lines exist and does not require a calibration pattern. Although the method requires at least three distorted lines residing in an image, it can cope with a situation in which fewer lines are found by adding more images taken by a same camera with different capturing angles. As long as there is a line involved in the scene, the method is applicable.

In order to increase the efficiency of UAVs, many airborne imaging systems use multi-sensor intersection and stitching technology. And coupled with the slight change of UAV flight attitude, it leads the airborne imaging system to work in inclined imaging mode. Compared with vertical imaging, inclined imaging has more complex geometric distortion and scale scaling problems. Direct mosaicking of the original image will lead to mosaic errors (such as misalignment artifacts or ''ghosting''). In addition, due to the change of UAVs' altitude and flight attitude, it will also lead to the change of ground objects such as rotation and zooming. Therefore, it is necessary to correct the trapezoidal distortion of inclined image in order to ensure the consistency of the scale of objects in the images to be stitched.

In view of the urgent need for high-resolution and high-precision infrared image data for geological environmental monitoring, we have developed a lightweight optical butting infrared imaging system for UAV to obtain infrared image data. When the system works, changes of UAVs flight attitude, altitude, imaging inclination, terrain fluctuation and other factors will cause great difficulties in image mosaicking. Hence, this paper studies the image precise geometric correction (including non-linear distortion correction of imaging system, inclined imaging trapezoidal distortion correction) of the system. In this paper, a robust mosaicking method combination of as-projective-as-possible warps and similarity transformation is proposed, which uses multiple images to generate a wide viewing field panorama. As shown in Figure 1, the research consists of three main steps. With the input of original images, a method based on division model [40] is used to achieve non-linear distortion correction; trapezoidal distortion correction is then put into force; the robust mosaicking strategy is applied to obtain the panorama. The details of the research content are discussed in the following sections.

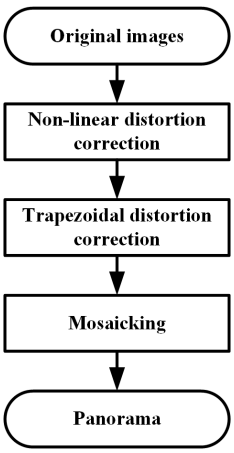

FIGURE 1. The overall flow charts of the research content.

The rest of the paper is structured as follows. Section II describes the method for image precise geometric correction. Section III describes the proposed robust mosaicking method combination of as-projective-as-possible warps and similarity transformation. Section IV evaluates the proposed robust mosaicking method comparing with the state-of-the-art mosaicking methods and present the panoramic mosaicking result for airborne lightweight optical butting infrared

imaging system. Finally, the paper presents conclusions in Section V.

II. METHOD FOR IMAGE GEOMETRIC CORRECTION

As UAV sensor platform, we used a DJI Matrice 600 UAV and a DJI RONIN-MX pan-tilt (SZ DJI Technology Company Ltd., China), which is very stable at low flight speed and low altitude. Moreover, our experimental system also consists of two lightweight infrared cameras, two data acquisition cards, a small single-board computer (Raspberry Pi) and an INS (Inertial Navigation System) with integrated GNSS (Global Navigation Satellite System) (SBG Ellipse2-N[3]). Key components in this system are shown in Figure 2. The technical details of Matrice 600, camera and Ellipse2-N are shown in Table 1.

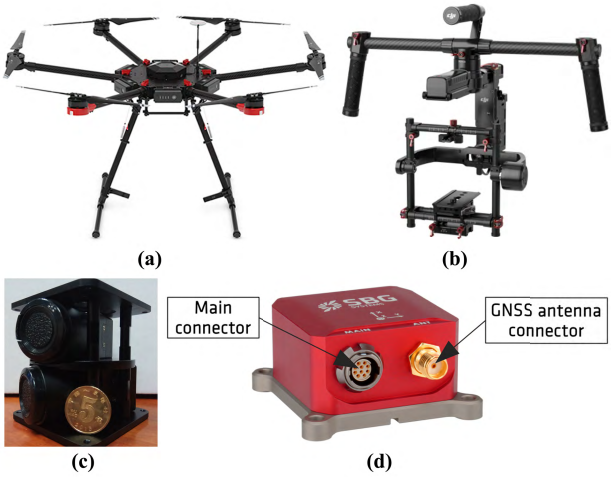

FIGURE 2. Key components in the experimental system. (a) DJI Matrice 600 UAV. (b) DJI RONIN-MX pan-tilt. (c) Lightweight optical butting infrared imaging system. (d) SBG Ellipse2-N.

Ellipse2-N includes an IMU (Inertial Measurement Unit) and runs an on-board enhanced EKF (Extended Kalman Filter). It works on single point mode and L1 GPS/GLONASS (Global Positioning System/GLObalnaya NAvigatsionnaya Sputnikovaya Sistema) fix quality in default, and provides both orientation and navigation data. We use it to acquire the longitude, latitude and elevation information of the imaging system in real-time and provide these to the Raspberry Pi to control the data acquisition cards to acquire digital images. At the same time, it also provides the attitude information of two cameras at imaging time. After obtaining the image sequence, non-linear distortion correction is performed first, then trapezoidal distortion correction is performed, and finally image mosaicking is performed.

A. NON-LINEAR DISTORTION CORRECTION

Fitzgibbon [40] proposed the division model as

$$\begin{cases} x_u = \dfrac{x_d}{1+\lambda_1 r_d^2+\lambda_2 r_d^4+\ldots} \\ y_u = \dfrac{y_d}{1+\lambda_1 r_d^2+\lambda_2 r_d^4+\ldots} \end{cases} \tag{1}$$

[3]https://www.sbg-systems.com/products/ellipse-2-series/

TABLE 1. Technical specifications of Matrice 600, camera and Ellipse2-N.

Component	Parameter	Value
Matrice 600	Symmetrical wheelbase (mm)	1133
	Weight (kg)	9.1
	Max. takeoff weight (kg)	6
	Max. horizontal velocity (m/s)	18
	Hovering time* (min)	16
	One battery capacity** (mAh)	4500
	Battery voltage (V)	22.2
Camera	Focal length (mm)	19
	Resolution	480×640
	Pixel size (um)	17
	Field of view (°)	30.9×24
	Max. frame rate (fps)	25
	Spectral range (um)	8∼14
	NETD*** (mk)	60
	Camera size (mm)	28×28×57
	Weight (g)	72
	Power consumption (W)	0.85
Ellipse2-N	Roll/pitch accuracy (RMS)	0.1°
	Heading accuracy (RMS)	< 0.5°
	Velocity accuracy (RMS)	0.1 m/s
	Horizontal position accuracy (RMS)	2.0 m
	Size (mm)	46×45×24
	Weight (g)	47
	Accelerometers range (g)	±16
	Gyroscopes range (°/s)	±450
	Input voltage (V)	5∼36
	Power consumption (W)	< 0.65
	GNSS receiver cold start time (s)	< 26
	GNSS receiver hot start time (s)	< 1
	GNSS output rate (Hz)	5

*: With max. takeoff weight.
**: Matrice 600 equipped with six batteries.
***: Noise Equivalent Temperature Difference.

where (x_u, y_u) and (x_d, y_d) are the corresponding coordinates of an undistorted point and a distorted point in an image, respectively. $r_d = \sqrt{(x_d - x_0)^2 + (y_d - y_0)^2}$ is the Euclidean distance of the distorted point to the distortion center (x_0, y_0). The division model is capable of expressing large distortion at much lower order. In particular, for many cameras a single parameter would suffice [40], [41]. In our study, we use the single parameter division model

$$\begin{cases} x_u = \dfrac{x_d}{1+\lambda r_d^2} \\ y_u = \dfrac{y_d}{1+\lambda r_d^2} \end{cases} \tag{2}$$

An equation of a straight line is expressed as

$$Ax_u + By_u + C = 0 \tag{3}$$

Refer to [39], we have

$$x_d^2 + y_d^2 + Dx_d + Ey_d + F = 0 \tag{4}$$

and

$$x_0^2 + y_0^2 + Dx_0 + Ey_0 + F - \frac{1}{\lambda} = 0 \tag{5}$$

Eq. (4) indicates that a group of parameter (D, E, F) can be determined by fitting a circle to an arc which is extracted from

an image. The circular arc in the image is projected from a straight line in the world. Extracting three arcs and determining three groups of parameter (D, E, F), then the distortion center can be estimated by solving the linear equations of

$$\begin{cases} (D_1 - D_2)x_0 + (E_1 - E_2)y_0 + (F_1 - F_2) = 0 \\ (D_1 - D_3)x_0 + (E_1 - E_3)y_0 + (F_1 - F_3) = 0 \end{cases} \tag{6}$$

and an estimate of λ can be obtained from

$$\lambda = \frac{1}{x_0^2 + y_0^2 + Dx_0 + Ey_0 + F} \tag{7}$$

The geometric calibration of each camera is carried out using the above-mentioned non-linear distortion calibration scheme. The obtained parameters are shown in Table 2, in which the effective focal length is obtained by using the known object space information and the corrected image information. The original image and corrected image are shown in Figure 3.

TABLE 2. Calibration parameters of lightweight optical butting infrared imaging system.

Parameter	Left camera	Right camera
λ	2.01924×10^{-8}	2.04753×10^{-8}
distortion center (x_0, y_0)	(241.7682, 318.8675)	(242.2211, 321.3967)
effective focal length (mm)	19.2094	19.1153

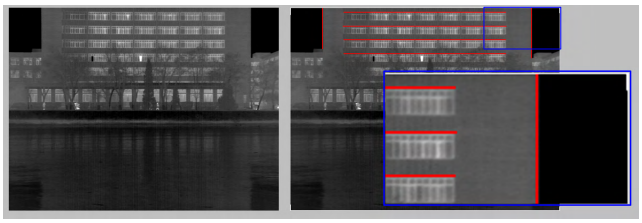

FIGURE 3. Original image and image after non-linear distortion correction. Some lines which are straight in the world have been annotated with red straight lines in the corrected image, showing strong vanishing points.

B. TRAPEZOIDAL DISTORTION CORRECTION

After correcting the non-linear distortion of the imaging system, this section only considers the trapezoidal distortion (imaging dip angle change) and scale scaling (altitude change) caused by the change of camera's exterior orientation elements. The scale scaling problem is solved in the process of image re-sampling. In this section, the original input image is the non-linear distortion corrected image, so it can be considered as an ideal aperture imaging. The object point, light center and image point satisfy the collinear equation. According to the imaging mode and pose information of the imaging system, the imaging geometry model is constructed, and then the trapezoidal distortion of the image is corrected by using the collinear equation. The coordinates involved in this section are shown in the Figure 4. $X_{wned}Y_{wned}Z_{wned}$ is

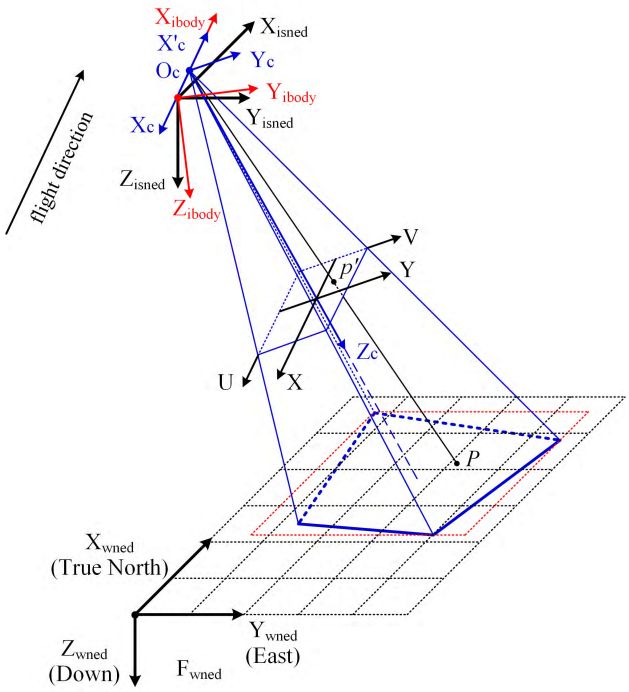

FIGURE 4. Principle diagram of trapezoidal distortion correction for single camera.

NED (North, East, Down) coordinates, which is LTP (Local Tangent Plane) coordinates. $X_{isned}Y_{isned}Z_{isned}$ is NED coordinates, which origin is the same as the sensor body coordinates $X_{ibody}Y_{ibody}Z_{ibody}$. O_c-$X_cY_cZ_c$ and O_c-$X'_cY_cZ_c$ are camera coordinates and camera auxiliary coordinates, respectively. X'_c axis is in the opposite direction of X_c axis. UV is the image coordinates. Trapezoidal distortion correction is projecting the original image under the UV coordinates to the NED coordinates, and then re-sample the projected image according to the ground resolution requirements to obtain the orthophoto image.

The current location informations obtained by Ellipse2-N are longitude, latitude and elevation in WGS84 (World Geodetic System 1984) coordinate (recorded as L, B and H, respectively). In order to calculate the position relationship between image sequence, it is necessary to transform location information into the coordinates in the Cartesian coordinates. The transformation relationship is as follow:

$$\begin{bmatrix} x_{ecef} \\ y_{ecef} \\ z_{ecef} \end{bmatrix} = \begin{bmatrix} (N+H)\cos B\cos L \\ (N+H)\cos B\sin L \\ [N(1-e^2)+H]\sin B \end{bmatrix} \tag{8}$$

where $e = \sqrt{(a^2-b^2)/a^2}$ is the first eccentricity of WGS84 coordinates reference ellipsoid, $a = 6378137\ m$ and $b = 6356752.3142\ m$ are the long and short half axle of ellipsoid, respectively. $N = a/\sqrt{1-e^2\sin^2 B}$ is the radius of curvature in prime vertical.

Because the Cartesian coordinates have larger values, the NED coordinates are more commonly used to describe

the position relationship in a small area. Let two points P_0 and P_1 exist in the small area, and the WGS84 coordinates are (L_0, B_0, H_0) and (L_1, B_1, H_1), respectively. The NED coordinates is established with P_0 as the origin, we have the rotation matrix from Cartesian coordinates to NED Coordinates

$$\boldsymbol{R}_{ecef2end} = \begin{bmatrix} -\cos L_0 \cos B_0 & -\sin L_0 \sin B_0 & \cos B_0 \\ -\sin L_0 & \cos L_0 & 0 \\ -\cos L_0 \cos B_0 & -\sin L_0 \cos B_0 & -\sin B_0 \end{bmatrix} \quad (9)$$

From Eq. (8), we have $(x_{0,ecef}, y_{0,ecef}, z_{0,ecef})$ and $(x_{1,ecef}, y_{1,ecef}, z_{1,ecef})$, then we have the NED ($P_0$ as the origin) coordinates of P_1

$$\begin{bmatrix} x_{1,ned} \\ y_{1,ned} \\ z_{1,ned} \end{bmatrix} = \boldsymbol{R}_{ecef2end} \begin{bmatrix} x_{1,ecef} - x_{0,ecef} \\ y_{1,ecef} - y_{0,ecef} \\ z_{1,ecef} - z_{0,ecef} \end{bmatrix} \quad (10)$$

When ideal aperture imaging, the NED coordinates $P(x_{wned}, y_{wned}, z_{wned})$ of object point has the following relationship with the UV coordinates $p'(u, v)$ of image point

$$z_c \begin{bmatrix} u \\ v \\ 1 \end{bmatrix} = \boldsymbol{M}_{IN}\boldsymbol{M}_{EX} \begin{bmatrix} x_{wned} \\ y_{wned} \\ 0 \\ 1 \end{bmatrix} = \begin{bmatrix} m_{11} & m_{12} & m_{13} & m_{14} \\ m_{21} & m_{22} & m_{23} & m_{24} \\ m_{31} & m_{32} & m_{33} & m_{34} \end{bmatrix} \begin{bmatrix} x_{wned} \\ y_{wned} \\ 0 \\ 1 \end{bmatrix} \quad (11)$$

where $\boldsymbol{M}_{IN}$ and $\boldsymbol{M}_{EX}$ are internal and external parameters matrix of camera, respectively. $\boldsymbol{M}_{IN}$ can be obtained after non-linear distortion correction.

The procedures of trapezoidal distortion correction are as follow.

Step 1: According to the position information obtained by Ellipse2-N when taking the i-th image, the translation $\boldsymbol{T}_{iws}$ between $X_{wned}Y_{wned}Z_{wned}$ coordinates and $X_{isned}Y_{isned}Z_{isned}$ coordinates is calculated. From Eq. (8), we have $(x_{0,ecef}, y_{0,ecef}, z_{0,ecef})$ and $(x_{i,ecef}, y_{i,ecef}, z_{i,ecef})$, then we have

$$\boldsymbol{T}_{iws} = -\boldsymbol{R}_{ecef2wned} \begin{bmatrix} x_{i,ecef} - x_{0,ecef} \\ y_{i,ecef} - y_{0,ecef} \\ z_{i,ecef} - z_{0,ecef} \end{bmatrix} \quad (12)$$

Step 2: According to the three Euler angles obtained by Ellipse2-N, the rotation matrix R_{isb} between $X_{isned}Y_{isned}Z_{isned}$ coordinates and $X_{ibody}Y_{ibody}Z_{ibody}$ coordinates is calculated

$$\boldsymbol{R}_{isb} = \begin{bmatrix} c_\psi c_\theta & c_\psi s_\theta s_\varphi + s_\psi c_\varphi & -c_\psi s_\theta c_\varphi + s_\psi s_\varphi \\ -s_\psi c_\theta & s_\psi s_\theta s_\varphi + c_\psi c_\varphi & s_\psi s_\theta c_\varphi + c_\psi s_\varphi \\ s_\theta & -c_\theta s_\varphi & c_\theta c_\varphi \end{bmatrix} \quad (13)$$

where φ, θ and ψ are roll, pitch and yaw angle between $X_{isned}Y_{isned}Z_{isned}$ coordinates and $X_{ibody}Y_{ibody}Z_{ibody}$ coordinates, respectively. $c* = \cos(*)$, $s* = \sin(*)$.

Step 3: The translation between $X_{ibody}Y_{ibody}Z_{ibody}$ coordinates and O_c-$X_c'Y_cZ_c$ coordinates is $(T_x, 0, 0)^T$. The rotation angle between $X_{ibody}Y_{ibody}Z_{ibody}$ coordinates and O_c-$X_c'Y_cZ_c$ coordinates is φ_x. $(T_x, 0, 0)^T$ and φ_x can be obtained by calibration at assembly time. Then, the NED coordinates of the object point corresponding to image point (u, v) in the original image can be calculated by the following formula

$$\begin{bmatrix} x_{wned} \\ y_{wned} \end{bmatrix} = \begin{bmatrix} um_{31} - m_{11} & um_{32} - m_{12} \\ vm_{31} - m_{21} & vm_{32} - m_{22} \end{bmatrix}^{-1} \begin{bmatrix} m_{14} - um_{34} \\ m_{24} - vm_{34} \end{bmatrix} \quad (14)$$

To verify the feasibility of the proposed method, we have performed experiments on image obtained by experimental system. Figure 5 shows the experimental results of ground simulation. Figure 6 shows the images after trapezoidal distortion correction.

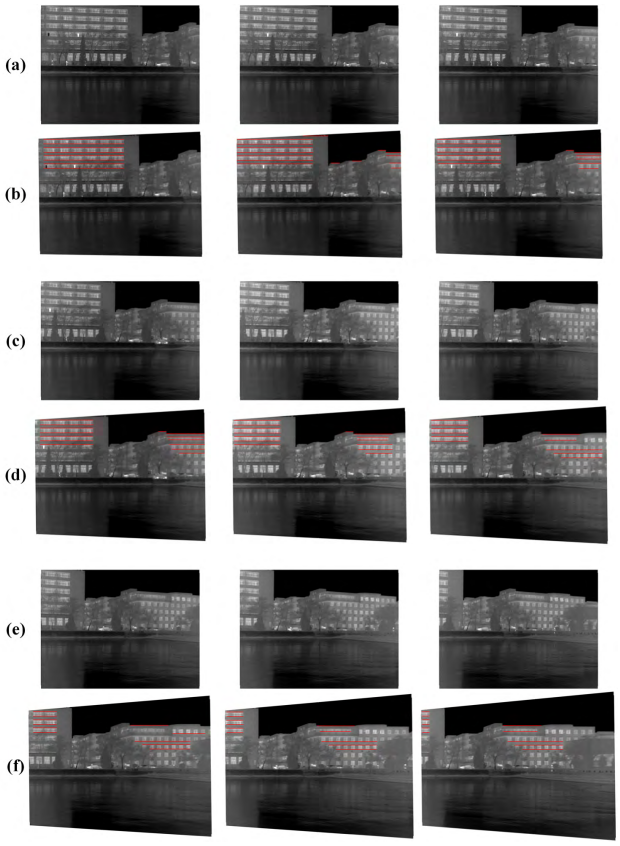

FIGURE 5. Experimental results of ground simulation. (a), (c) and (e) are original images. (b), (d) and (f) are images after trapezoidal distortion correction corresponding to (a), (c) and (e), respectively.

III. ROBUST MOSAICKING METHOD

Image mosaicking is the process of combining a set of images into a larger image. The result shows a wider field of view. A basic approach to image mosaicking is using feature matching to robustly estimate a global transformation. Given two images, extracting features and matching them to obtain a set

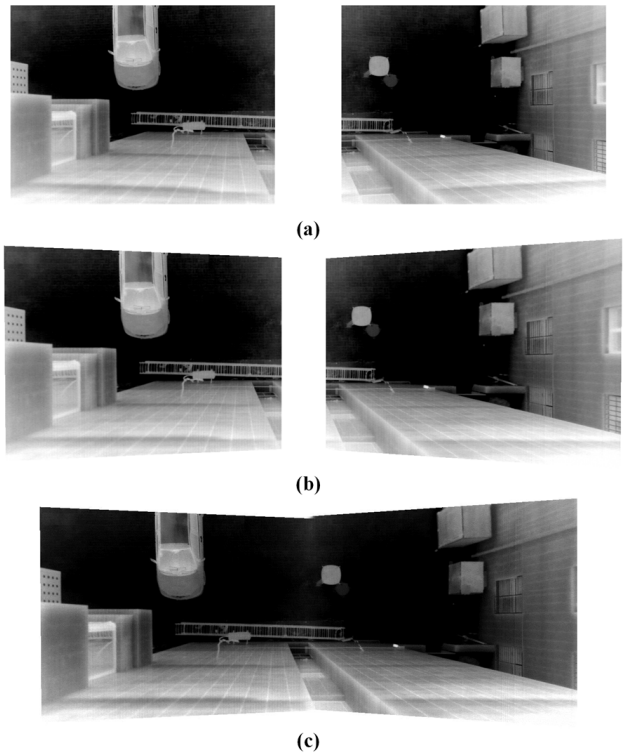

FIGURE 6. Experimental result. (a) Original images. (b) Images after trapezoidal distortion correction. (c) Optical butting effect.

of matching pairs. Then, removing the outliers and fitting a global transformation by geometric verification such as RANSAC (RANdom SAmple Consensus) [46]. This transformation describes the geometric relationships of the overlapping regions between two images. In most cases, estimate a projective transformation (or say homography) because it is the most flexible global transformation. After that, one of the images is warped by the projective transformation to bring them into alignment. Finally, image compositing is performed to generate the final result. But, there are two problems in the projective warp. The first one is local misalignment. Projective transformation is not flexible enough to achieve accurate alignment on the overlapping regions. The second problem is distortion, which appears on the non-overlapping regions. In particular, projective transformations introduce shape distortion and area distortion (appears as severely stretched and enlarged at the edge of the image).

A. AS-PROJECTIVE-AS-POSSIBLE WARPS

Recently, several local warp methods are proposed to provide better alignment. One of the state of the art methods is the APAP (As-Projective-As-Possible) warps, proposed by Zaragoza *et al*. [28]. Warping function can be expressed as w: $(x, y) \rightarrow (x', y')$. Let $\boldsymbol{x} = [x, y]^T$ and $\boldsymbol{x}' = [x', y']^T$ be matching points across overlapping images I and I', the projective warp following the relation

$$\bar{\boldsymbol{x}}' = \boldsymbol{H}\bar{\boldsymbol{x}} = \begin{bmatrix} h_1 & h_2 & h_3 \\ h_4 & h_5 & h_6 \\ h_7 & h_8 & 1 \end{bmatrix} \bar{\boldsymbol{x}} \tag{15}$$

where $\bar{\boldsymbol{x}} = [x, y, 1]^T$ and $\bar{\boldsymbol{x}}' = [x', y', 1]^T$, $\boldsymbol{H}$ defines the homography. Eq. (15) can also be expressed in another form

$$\begin{cases} x' = H_x(x, y) = \dfrac{h_1 x + h_2 y + h_3}{h_7 x + h_8 y + 1} \\ y' = H_y(x, y) = \dfrac{h_4 x + h_5 y + h_6}{h_7 x + h_8 y + 1} \end{cases} \tag{16}$$

For a set of point matches $\{\boldsymbol{x}_i, \boldsymbol{x}_i'\}(i = 1, 2, \ldots, N)$, DLT (Direct Linear Transformation) method [47] is used to estimate $\boldsymbol{H}$

$$\boldsymbol{0}_{3\times 1} = \begin{bmatrix} \boldsymbol{0}_{1\times 3} & -\bar{\boldsymbol{x}}^T & y'\bar{\boldsymbol{x}}^T \\ \bar{\boldsymbol{x}}^T & \boldsymbol{0}_{1\times 3} & -x'\bar{\boldsymbol{x}}^T \\ -y'\bar{\boldsymbol{x}}^T & x'\bar{\boldsymbol{x}}^T & \boldsymbol{0}_{1\times 3} \end{bmatrix} \boldsymbol{h} \tag{17}$$

where $\boldsymbol{h} = [h_1, h_2, h_1, h_2, h_1, h_2, h_1, h_2, 1]^T$. Let $\boldsymbol{d}_i$ be the first-two rows of the 3×9 matrix in Eq. (17) computed for the i-th point match $\{\boldsymbol{x}_i, \boldsymbol{x}_i'\}$. Then, for global projective transformation we have

$$\tilde{\boldsymbol{h}} = \underset{\boldsymbol{h}}{argmin} \sum_{i=1}^{N} \|\boldsymbol{d}_i \boldsymbol{h}\|^2 \quad s.t. \|\boldsymbol{h}\| = 1 \tag{18}$$

In order to weaken the local misalignment caused by parallax errors in overlapping regions of images, APAP warps uses a location dependent homography $\boldsymbol{H}_*$

$$\tilde{\boldsymbol{h}}_* = \underset{\boldsymbol{h}}{argmin} \sum_{i=1}^{N} \|\omega_*^i \boldsymbol{d}_i \boldsymbol{h}\|^2 \quad s.t. \|\boldsymbol{h}\| = 1 \tag{19}$$

The scalar weights ω_*^i(i, 1, 2, …, N) are calculated as

$$\omega_*^i = max\left(exp\left(-\|\boldsymbol{x}_* - \boldsymbol{x}_i\|^2/\sigma^2\right), \gamma\right) \tag{20}$$

where σ is a scale parameter (here, $\sigma = 8.5$), and γ is a threshold parameter to prevent the weights to be too sparse (here, $\gamma = 0.1$).

B. PROJECTIVE-SIMILARITY TRANSFORMATION

APAP warps locally adapts to different transformations on the overlapping regions. Compared with projective transformation, APAP warps achieves better alignment on the overlapping regions. However, for the non-overlapping regions, it is still a projective transformation. Observing that the distortion issue is not resolved, we want to design a better warping function for image mosaicking. Similarity transformation does not introduce any shape distortion nor area distortion. It is composed of scaling, rotation and translation, therefore no shapes are squeezed or stretched. Also, there is no non-uniform scaling. Refer to [48] rotate the original coordinates to form the new coordinates

$$\begin{bmatrix} x \\ y \\ 1 \end{bmatrix} = \begin{bmatrix} \cos\theta & -\sin\theta & 0 \\ \sin\theta & \cos\theta & 0 \\ 0 & 0 & 1 \end{bmatrix} \begin{bmatrix} u \\ v \\ 1 \end{bmatrix} = \boldsymbol{R} \begin{bmatrix} u \\ v \\ 1 \end{bmatrix} \tag{21}$$

where $\theta = atan2(h_8, -h_7)$. Then, Eq. (15) can be rewritten as

$$\begin{bmatrix} x' \\ y' \\ 1 \end{bmatrix} = \begin{bmatrix} \hat{h}_1 & \hat{h}_2 & \hat{h}_3 \\ \hat{h}_4 & \hat{h}_5 & \hat{h}_6 \\ -c & 0 & 1 \end{bmatrix} \begin{bmatrix} u \\ v \\ 1 \end{bmatrix} = \hat{\boldsymbol{R}} \begin{bmatrix} u \\ v \\ 1 \end{bmatrix} \tag{22}$$

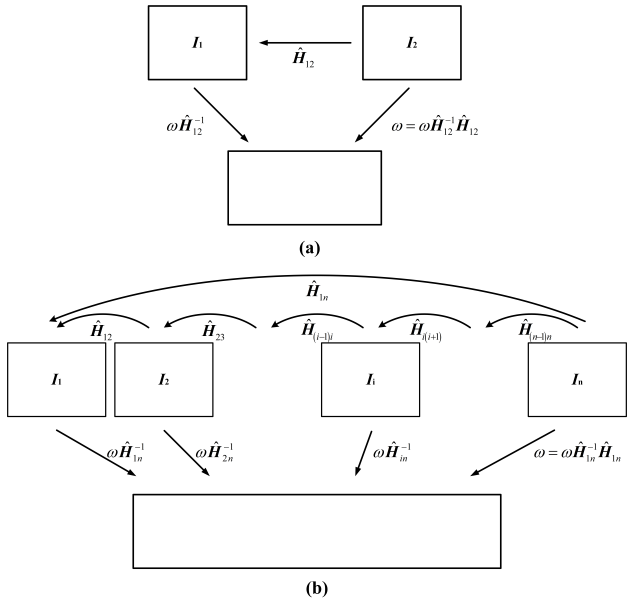

FIGURE 7. Geometric transformation relation for Projective-Similarity Transformation. (a) Two images. (b) Image sequence.

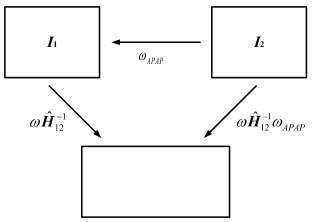

FIGURE 8. Geometric transformation relation for the proposed method.

where $c = \sqrt{h_7^2 + h_8^2}$. Then, warping function can be expressed as

$$H(u, v) = \begin{bmatrix} H_x(x, y) \\ H_y(x, y) \end{bmatrix} = \begin{bmatrix} \dfrac{\hat{h}_1 u + \hat{h}_2 v + \hat{h}_3}{1 - cu} \\ \dfrac{\hat{h}_4 u + \hat{h}_5 v + \hat{h}_6}{1 - cu} \end{bmatrix} \tag{23}$$

When u is a constant u_0, Eq. (23) can be rewritten as

$$\begin{cases} x' = H_x(x, y) = \dfrac{\hat{h}_2}{1 - cu_0} v + \dfrac{\hat{h}_1 u_0 + \hat{h}_3}{1 - cu_0} \\ y' = H_y(x, y) = \dfrac{\hat{h}_5}{1 - cu_0} v + \dfrac{\hat{h}_4 u_0 + \hat{h}_6}{1 - cu_0} \end{cases} \tag{24}$$

It can be seen that for a line parallel to the v axis, the length ratio of the line segment can still be maintained after transformation, that is a similarity transformation.

Based on the above analysis, projection-similarity transformation can be constructed, and the image to be mosaicked can be divided into two regions: overlapping region uses projection transformation function $H(u, v)$, and non-overlapping region uses similarity transformation function $S(u, v)$. Refer to Eq. (24) and the concept of ruled surface [49], $S(u, v)$ can

TABLE 3. The processing times of three sequences of images, the unit in the table is second.

	First sequenc	Second sequence	Third sequence
AutoStitch	1.3520	2.2173	2.8117
ICE	-	4.5729	4.2039
Global homography	5.4979	17.8927	10.6627
APAP	7.3354	21.6863	14.4697
Projective-similarity	5.6352	18.6241	11.3990
Proposed	8.9176	24.0653	16.3148

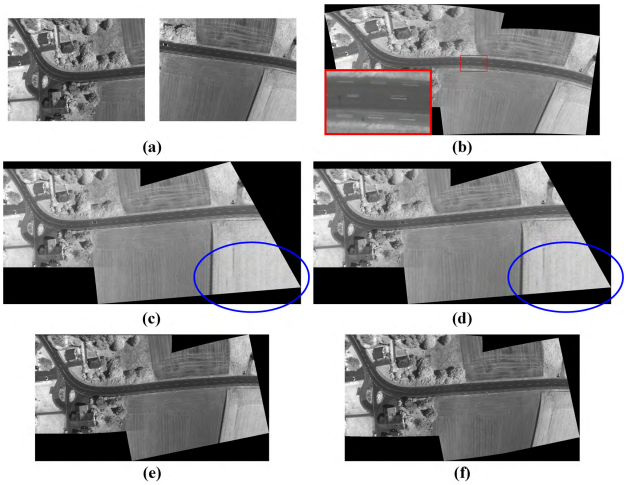

FIGURE 9. The generated panoramas for first sequence images (960×1280). (a) Original images. (b) AutoStitch. (c) Global homography transformation. (d) APAP warps. (e) Projective-similarity transformation. (f) the proposed method.

be obtained as follow:

$$S(u, v) = \frac{1}{1 - cu_0} \left\{ \begin{bmatrix} \hat{h}_5 & \hat{h}_2 \\ -\hat{h}_2 & \hat{h}_5 \end{bmatrix} \begin{bmatrix} u \\ v \end{bmatrix} + \begin{bmatrix} (\hat{h}_1 - \hat{h}_5)u_0 + \hat{h}_3 \\ (\hat{h}_4 + \hat{h}_2)u_0 + \hat{h}_6 \end{bmatrix} \right\} \tag{25}$$

As shown in Figure 7, the geometric transformation relation for image mosaicking is given.

C. COMBINATION APAP WARPS AND SIMILARITY TRANSFORMATION

APAP warps achieves better alignment on the overlapping regions. Similarity transformation greatly reduces the distortions on the non-overlapping regions. Combination APAP warps and similarity transformation can be achieved the best of both worlds. As shown in Figure 8, replacing projection transformation in Figure 7 with APAP warps can achieved this strategy. Refer to [28], we uniformly partition the images into a grid of 40×40 cells. Then, images are divided into overlapping and non-overlapping region according to the feature matching result. The resulting warp gradually changes from APAP warps to a similarity transformation.

IV. EXPERIMENTAL EVALUATION

In order to verify the validity and accuracy of the proposed image mosaicking method, a lot of experiments

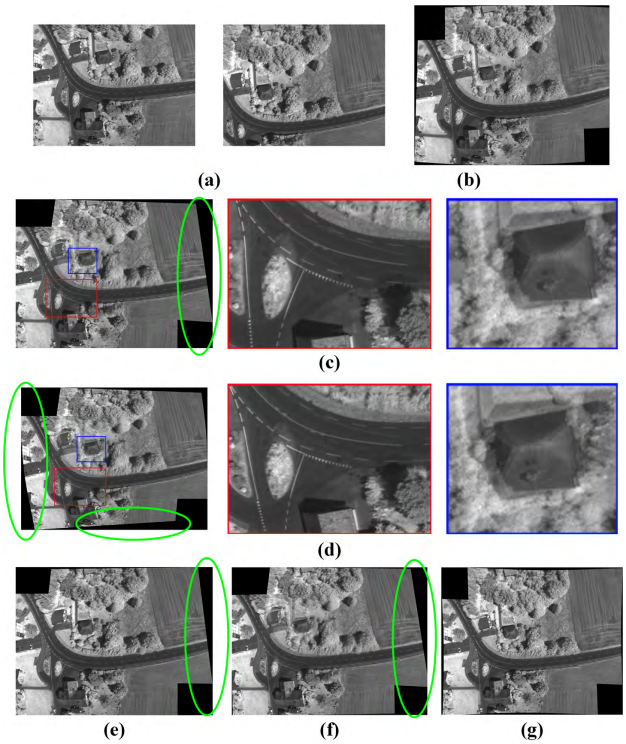

FIGURE 10. The generated panoramas for second sequence images (960×1280). (a) Original images. (b) AutoStitch. (c) Global homography transformation. (d) Projective-similarity transformation. (e) ICE. (f) APAP warps. (g) the proposed method.

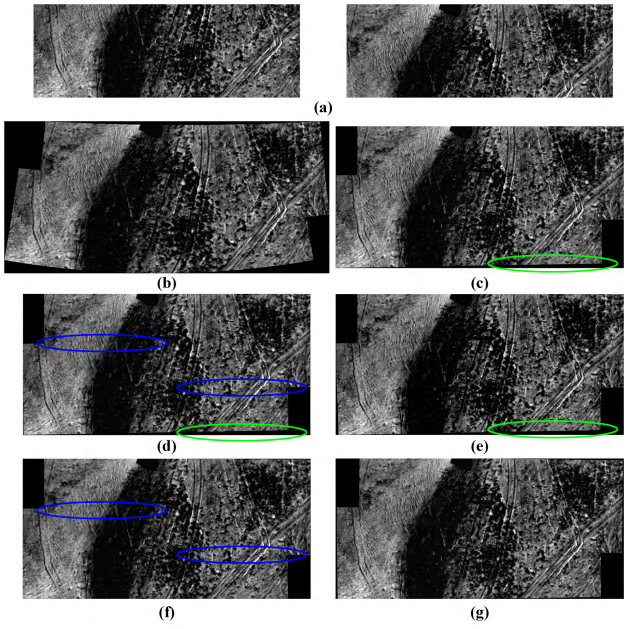

FIGURE 11. The generated panoramas for third sequence images (447×1277). (a) Original images. (b) AutoStitch. (c) ICE. (d) Global homography transformation. (e) APAP warps. (f) Projective-similarity transformation. (g) the proposed method.

have been carried out in this paper. We compare the proposed method with AutoStitch, ICE, global homography transformation, APAP warps and projective-similarity transformation. We implemented the proposed method,

FIGURE 12. Panoramic mosaics of airborne images generated by AutoStitch.

global homography transformation, APAP warps and projective-similarity transformation using MATLAB R2014b and ran experiments on a PC with Intel(R) Core(TM) i7-5960X CPU @ 3.00GHz and 32GB RAM. We used the VLFeat(VisionLab Features)[4] [50] to extract SIFT features and performed matching with FLANN (Fast Library for Approximate Nearest Neighbors)[5] [51] and RANSAC for obtaining the projective transformation for the overlapping regions.

A. EXPERIMENTAL EVALUATION

While many data have been tested (including those used elsewhere) with convincing results, only a few can be included in this paper. Here we show three series of experiments on image mosaicking. The processing times of three sequences of images for different methods are given in Table 3. Experimental results are shown in Figure 9∼11.

From Figure 9, the result of AutoStitch has ''ghosting'' phenomenon, indicating that AutoStitch's ability to handle parallax is weak. For ICE, images were unsuccessful generated panorama. ICE considers that there is non-overlapping region between the two images. The result of global homography transformation has ''ghosting'', shape distortion and

[4]http://www.vlfeat.org/
[5]http://www.cs.ubc.ca/research/flann/

FIGURE 13. Panoramic mosaics of airborne images generated by ICE.

FIGURE 14. Panoramic mosaics of airborne images generated by the proposed method.

area distortion. The APAP warps weakens ''ghosting'' phenomenon of global homography transformation, but it still has to shape distortion and area distortion, as shown in the blue ellipse marked. Projective-similarity transformation weakens the shape distortion, but it always has a slight ''ghosting'' phenomenon. The proposed method weakens both the ''ghosting'', shape distortion and area distortion.

From Figure 10, the results of global homography transformation and projective-similarity transformation have ''ghosting'', shape distortion and area distortion. The results of ICE have shape distortion and area distortion. APAP warps weakens ''ghosting'' phenomenon of global homography transformation, but it still has to shape distortion and area distortion, as showed in the green ellipse marked. The proposed method weakens both the ''ghosting'', shape distortion and area distortion.

From Figure 11, AutoStitch adopts spherical projection for image warping. The results of ICE, global homography transformation and APAP have shape distortion and area distortion, as showed in the green ellipse marked. There are seams in the blue ellipse marked. The proposed method weakens both the shape distortion and area distortion.

B. PANORAMIC MOSAICS OF AIRBORNE IMAGES

Here, Figure 12∼14 shows the results of AutoStitch, ICE and the proposed image mosaicking method for airborne lightweight optical butting infrared imaging system. Only image mosaicking takes 9.0128, 33.6129 and 132.4973 seconds, respectively. Since AutoStitch adopts spherical projection for image warping, therefore overlapping regions exist ''ghosting''. Although there is no ''ghosting'' in ICE result, there is stretched and enlarged at the edge of the images. Can be seen that the proposed method introduce much less distortions in terms of shape and area. The relative altitude is 80 m, and the experimental area has obvious topographic fluctuations, with the maximum elevation difference of about 6 m.

V. CONCLUSION

In this paper, we proposed a robust mosaicking method combination of as-projective-as-possible warps and similarity transformation. It is developed basing on an analysis of projective transformation and similarity transformation. The proposed method simultaneously takes into consideration

the flexibility of alignment and the preservation of image shapes. Intuitively, on the overlapping regions, it performs an as-projective-as-possible warps. On the non-overlapping regions, it gradually becomes a similarity warp. One possible future direction is to optimize computational speed. In the future, we would also wish to explore the possibility of adopting the proposed method to different applications.

REFERENCES

[1] Q. Yang and S.-J. Yoo, "Optimal UAV path planning: Sensing data acquisition over IoT sensor networks using multi-objective bio-inspired algorithms," *IEEE Access*, vol. 6, pp. 13671–13684, 2018. doi: 10.1109/ACCESS.2018.2812896.

[2] C. Hu, Z. Zhang, Y. Tao, and N. Wang, "Decentralized real-time estimation and tracking for unknown ground moving target using UAVs," *IEEE Access*, vol. 7, pp. 1808–1817, 2018. doi: 10.1109/ACCESS.2018.2885776.

[3] T. Yang, Z. Li, F. Zhang, B. Xie, J. Li, and L. Liu, "Panoramic UAV surveillance and recycling system based on structure-free camera array," *IEEE Access*, vol. 7, pp. 25763–25778, 2019. doi: 10.1109/ACCESS.2019.2900167.

[4] Z. Xiao, B. Zhu, Y. Wang, and P. Miao, "Low-complexity path planning algorithm for unmanned aerial vehicles in complicated scenarios," *IEEE Access*, vol. 6, pp. 57049–57055, 2018. doi: 10.1109/ACCESS.2018.2873084.

[5] M. Wieser, G. Mandlburger, M. Hollaus, J. Otepka, P. Glira, and N. Pfeifer, "A case study of UAS borne laser scanning for measurement of tree stem diameter," *Remote Sens.*, vol. 9, no. 11, p. 1154, Nov. 2017. doi: 10.3390/rs9111154.

[6] J. Suomalainen, N. Anders, S. Iqbal, G. Roerink, J. Franke, P. Wenting, D. Hünniger, H. Bartholomeus, R. Becker, and L. Kooistra, "A lightweight hyperspectral mapping system and photogrammetric processing chain for unmanned aerial vehicles," *Remote Sens.*, vol. 6, no. 11, pp. 11013–11030, 2014. doi: 10.3390/rs61111013.

[7] F. Deng, X. Zhu, X. Li, and M. Li, "3D digitisation of large-scale unstructured Great Wall heritage sites by a small unmanned helicopter," *Remote Sens.*, vol. 9, no. 5, p. 423, Apr. 2017. doi: 10.3390/rs9050423.

[8] M. B. Bejiga, A. Zeggada, A. Nouffidj, and F. Melgani, "A convolutional neural network approach for assisting avalanche search and rescue operations with UAV imagery," *Remote Sens.*, vol. 9, no. 2, p. 100, Jan. 2017. doi: 10.3390/rs9020100.

[9] C.-C. Liu, P.-L. Chen, T. Matsuo, and C.-Y. Chen, "Rapidly responding to landslides and debris flow events using a low-cost unmanned aerial vehicle," *Proc. SPIE*, vol. 9, no. 1, Aug. 2015, Art. no. 096016. doi: 10.1117/1.JRS.9.096016.

[10] F. Wu, X. Wang, H. Wei, J. Liu, F. Liu, and J. Yang, "Panoramic mosaics from Chang'E-3 PCAM images at point A," *Remote Sens.*, vol. 8, no. 10, p. 812, Sep. 2016. doi: 10.3390/rs8100812.

[11] J. Zheng, Z. Zhang, Q. Tao, K. Shen, and Y. Wang, "An accurate multi-row panorama generation using multi-point joint stitching," *IEEE Access*, vol. 6, pp. 27827–27839, 2018. doi: 10.1109/ACCESS.2018.2829082.

[12] K. Chen, J. Tu, J. Yao, and J. Li, "Generalized content-preserving warp: Direct photometric alignment beyond color consistency," *IEEE Access*, vol. 6, pp. 69835–69849, 2018. doi: 10.1109/ACCESS.2018.2877794.

[13] C.-H. Chang, Y. Sato, and Y.-Y. Chuang, "Shape-preserving half-projective warps for image stitching," in *Proc. IEEE Conf. Comput. Vis. Pattern Recognit. (CVPR)*, Columbus, OH, USA, Jun. 2014, pp. 3254–3261. doi: 10.1109/CVPR.2014.422.

[14] C. C. Lin, S. U. Pankanti, K. N. Ramamurthy, and A. Y. Aravkin, "Adaptive as-natural-as-possible image stitching," in *Proc. IEEE Conf. Comput. Vis. Pattern Recognit. (CVPR)*, Boston, MA, USA, Jun. 2015, pp. 1155–1163. doi: 10.1109/CVPR.2015.7298719.

[15] Y.-S. Chen and Y.-Y. Chuang, "Natural image stitching with the global similarity prior," in *Proc. Eur. Conf. Comput. Vis. (ECCV)*, Amsterdam, The Netherland, 2016, pp. 186–201. doi: 10.1007/978-3-319-46454-1_12.

[16] T.-Z. Xiang, G.-S. Xia, X. Bai, and L. Zhang, "Image stitching by line-guided local warping with global similarity constraint," *Pattern Recognit.*, vol. 83, pp. 481–497, Nov. 2018. doi: 10.1016/j.patcog.2018.06.013.

[17] J. F. Bell, III *et al.*, "Pancam multispectral imaging results from the Spirit rover at Gusev crater," *Science*, vol. 305, no. 5685, pp. 800–806, Aug. 2004. doi: 10.1126/science.1100175.

[18] J. F. Bell, III *et al.*, "Pancam multispectral imaging results from the Opportunity rover at Meridiani planum," *Science*, vol. 306, no. 5702, pp. 1703–1709, Dec. 2004. doi: 10.1126/science.1105245.

[19] D. F. Blake *et al.*, "Curiosity at Gale crater, Mars: Characterization and analysis of the Rocknest sand shadow," *Science*, vol. 341, no. 6153, p. 1239505, Sep. 2013. doi: 10.1126/science.1239505.

[20] J. P. Grotzinger *et al.*, "A habitable fluvio-lacustrine environment at Yellowknife bay, Gale crater, Mars," *Science*, vol. 343, no. 6169, Jan. 2014, Art. no. 1242777. doi: 10.1126/science.1242777.

[21] H.-Y. Shum, K.-T. Ng, and S.-C. Chan, "A virtual reality system using the concentric mosaic: Construction, rendering, and data compression," *IEEE Trans. Multimedia*, vol. 7, no. 1, pp. 85–95, Feb. 2005. doi: 10.1109/TMM.2004.840591.

[22] C.-W. Ngo, T.-C. Pong, and H.-J. Zhang, "Motion analysis and segmentation through spatio-temporal slices processing," *IEEE Trans. Image Process.*, vol. 12, no. 3, pp. 341–355, Mar. 2003. doi: 10.1109/TIP.2003.809020.

[23] Y. Ma, L. Wang, A. Y. Zomaya, D. Chen, and R. Ranjan, "Task-tree based large-scale mosaicking for massive remote sensed imageries with dynamic DAG scheduling," *IEEE Trans. Parallel Distrib. Syst.*, vol. 25, no. 8, pp. 2126–2137, Aug. 2014. doi: 10.1109/TPDS.2013.272.

[24] S. Saito, R. Arai, and Y. Aoki, "Seamline determination based on semantic segmentation for aerial image mosaicking," *IEEE Access*, vol. 3, pp. 2847–2856, 2015. doi: 10.1109/ACCESS.2015.2508921.

[25] W. Jing, S. Huo, Q. Miao, and X. Chen, "A model of parallel mosaicking for massive remote sensing images based on spark," *IEEE Access*, vol. 5, pp. 18229–18237, 2017. doi: 10.1109/ACCESS.2017.2746098.

[26] M. Brown and D. G. Lowe, "Automatic panoramic image stitching using invariant features," *Int. J. Comput. Vis.*, vol. 74, no. 1, pp. 59–73, Aug. 2007. doi: 10.1007/s11263-006-0002-3.

[27] J. Gao, S. J. Kim, and M. S. Brown, "Constructing image panoramas using dual-homography warping," in *Proc. IEEE Conf. Comput. Vis. Pattern Recognit. (CVPR)*, Colorado Springs, CO, USA, Jun. 2011, pp. 49–56. doi: 10.1109/CVPR.2011.5995433.

[28] J. Zaragoza, T.-J. Chin, Q.-H. Tran, M. S. Brown, and D. Suter, "As-projective-as-possible image stitching with moving DLT," *IEEE Trans. Pattern Anal. Mach. Intell.*, vol. 36, no. 7, pp. 1285–1298, Jul. 2013. doi: 10.1109/TPAMI.2013.247.

[29] D. G. Lowe, "Object recognition from local scale-invariant features," in *Proc. IEEE Conf. Comput. Vis. (ICCV)*, Kerkyra, Greece, Sep. 1999, pp. 1150–1157. doi: 10.1109/ICCV.1999.790410.

[30] D. G. Lowe, "Distinctive image features from scale-invariant keypoints," *Int. J. Comput. Vis.*, vol. 60, no. 2, pp. 91–110, 2004. doi: 10.1023/B:VISI.0000029664.99615.94.

[31] J. Ma, X. Jiang, J. Jiang, J. Zhao, and X. Guo, "LMR: Learning a two-class classifier for mismatch removal," *IEEE Trans. Image Process.*, vol. 28, no. 8, pp. 4045–4059, Aug. 2019. doi: 10.1109/TIP.2019.2906490.

[32] L. Zhang, L. Zhang, B. Du, J. You, and D. Tao, "Hyperspectral image unsupervised classification by robust manifold matrix factorization," *Inf. Sci.*, vol. 485, pp. 154–169, Jun. 2019. doi: 10.1016/j.ins.2019.02.008.

[33] Z. Wang, B. Du, W. Tu, L. Zhang, and D. Tao, "Incorporating distribution matching into uncertainty for multiple kernel active learning," *IEEE Trans. Knowl. Data Eng.*, to be published. doi: 10.1109/TKDE.2019.2923211.

[34] Y. Wu, B. Jiang, and N. Lu, "A descriptor system approach for estimation of incipient faults with application to high-speed railway traction devices," *IEEE Trans. Syst., Man, Cybern., Syst.*, to be published. doi: 10.1109/TSMC.2017.2757264.

[35] J. Ma, J. Zhao, J. Tian, A. L. Yuille, and Z. Tu, "Robust point matching via vector field consensus," *IEEE Trans. Image Process.*, vol. 23, no. 4, pp. 1706–1721, Apr. 2014. doi: 10.1109/TIP.2014.2307478.

[36] J. Ma, H. Zhou, J. Zhao, Y. Gao, J. Jiang, and J. Tian, "Robust feature matching for remote sensing image registration via locally linear transforming," *IEEE Trans. Geosci. Remote Sens.*, vol. 53, no. 12, pp. 6469–6481, Dec. 2015. doi: 10.1109/TGRS.2015.2441954.

[37] J. Ma, J. Zhao, J. Jiang, H. Zhou, and X. Guo, "Locality preserving matching," *Int. J. Comput. Vis.*, vol. 127, no. 5, pp. 512–531, 2019. doi: 10.1007/s11263-018-1117-z.

[38] F.-L. Wu, J.-J. Liu, X. Ren, and C. Li, "Deep space exploration panoramic camera calibration technique based on circular markers," *Acta Optica Sinica*, vol. 33, no. 11, Nov. 2013, Art. no. 1115002. doi: 10.3788/AOS201333.1115002.

[39] F. Wu, H. Wei, and X. Wang, "Correction of image radial distortion based on division model," *Proc. SPIE*, vol. 56, no. 1, Jan. 2017, Art. no. 013108. doi: 10.1117/1.OE.56.1.013108.

[40] A. W. Fitzgibbon, "Simultaneous linear estimation of multiple view geometry and lens distortion," in *Proc. IEEE Conf. Comput. Vis. Pattern Recognit. (CVPR)*, Kauai, HI, USA, Dec. 2001, p. 1. doi: 10.1109/CVPR.2001.990465.
[41] D. Claus and A. W. Fitzgibbon, "A rational function lens distortion model for general cameras," in *Proc. IEEE Conf. Comput. Vis. Pattern Recognit. (CVPR)*, San Diego, CA, USA, Jun. 2005, pp. 213–219. doi: 10.1109/CVPR.2005.43.
[42] R. Hartley and S. B. Kang, "Parameter-free radial distortion correction with center of distortion estimation," *IEEE Trans. Pattern Anal. Mach. Intell.*, vol. 29, no. 8, pp. 1309–1321, Aug. 2007. doi: 10.1109/TPAMI.2007.1147.
[43] B. Prescott and G. F. Mclean, "Line-based correction of radial lens distortion," *Graph. Models Image Process.*, vol. 59, pp. 39–47, Jan. 1997. doi: 10.1006/gmip.1996.0407.
[44] F. Devernay and O. Faugeras, "Straight lines have to be straight," *Mach. Vis. Appl.*, vol. 13, no. 1, pp. 14–21, Aug. 2001. doi: 10.1007/PL00013269.
[45] M. Ahmed and A. Farag, "Nonmetric calibration of camera lens distortion: Differential methods and robust estimation," *IEEE Trans. Image Process.*, vol. 14, no. 8, pp. 1215–1230, Aug. 2005. doi: 10.1109/TIP.2005.846025.
[46] M. A. Fischler and R. Bolles, "Random sample consensus: A paradigm for model fitting with applications to image analysis and automated cartography," *Commun. ACM*, vol. 24, no. 6, pp. 381–395, 1981. doi: 10.1145/358669.358692.
[47] Z. Zhang, "Parameter estimation techniques: A tutorial with application to conic fitting," *Image Vis. Comput.*, vol. 15, no. 1, pp. 59–76, 1997. doi: 10.1016/S0262-8856(96)01112-2.
[48] O. Chum, T. Pajdla, and P. Sturm, "The geometric error for homographies," *Comput. Vis. Image Understand.*, vol. 97, no. 1, pp. 86–102, Jan. 2005. doi: 10.1016/j.cviu.2004.03.004.
[49] V. A. Toponogov, *Differential Geometry of Curves and Surfaces: A Concise Guide*. Boston, MA, USA: Birkhaüser, 2006, pp. 102–105.
[50] A. Vedaldi and B. Fulkerson, "Vlfeat: An open and portable library of computer vision algorithms," in *Proc. 18th ACM Int. Conf. Multimedia (MM)*, Firenze, Italy, 2010, pp. 1469–1472.
[51] M. Muja and D. G. Lowe, "Scalable nearest neighbor algorithms for high dimensional data," *IEEE Trans. Pattern Anal. Mach. Intell.*, vol. 36, no. 11, pp. 2227–2240, Nov. 2014. doi: 10.1109/TPAMI.2014.2321376.

FANLU WU was born in 1988. He received the B.S. degree in measurement and control technology and instruments from the Changchun University of Science and Technology, Changchun, China, in 2011, the M.S. degree in astronomical techniques and methodology from the University of the Chinese Academy of Sciences, Beijing, China, in 2014, and the Ph.D. degree in instruments science and technology from Tianjin University, Tianjin, China, in 2018. Since 2018, he has been an Assistant Professor with the Changchun Institute of Optics, Fine Mechanics and Physics, Chinese Academy of Sciences. His research interests include computer vision, remote sensing, and planetary exploration.

HAINAN GUAN was born in 1990. He received the B.S. degree in electronic science and technology and the M.S. degree in control science and engineering from the Huazhong University of Science and Technology, Wuhan, China, in 2014 and 2017, respectively. Since 2017, he has been an Assistant Professor with the Changchun Institute of Optics, Fine Mechanics and Physics, Chinese Academy of Sciences. His research interests include image processing and circuit design in space science.

DEJIE YAN was born in 1979. She received the B.S. degree in measurement and control technology and instruments from Jilin University, Changchun, China, in 2003, and the M.S. degree in optical engineering from the Graduate School of Chinese Academy of Sciences, Beijing, China, in 2010. She is currently an Associate Professor with the Changchun Institute of Optics, Fine Mechanics and Physics, Chinese Academy of Sciences. Her research interests include image processing and circuit design in space science.

ZHENG WANG was born in 1987. He received the B.S. degree in communication engineering and the M.S. degree in signal and information processing from Jilin University, Changchun, China, in 2010 and 2013, respectively. Since 2018, he has been an Assistant Professor with the Changchun Institute of Optics, Fine Mechanics and Physics, Chinese Academy of Sciences. His research interests include electronic design, remote sensing, and image processing.

DONG WANG was born in 1979. He received the B.S. degree in photoelectric information engineering from the Changchun University of Science and Technology, Changchun, China, in 2002, and the Ph.D. degree in mechatronic engineering from the Graduate School of Chinese Academy of Sciences, Beijing, China, in 2007. He is currently a Professor with the Changchun Institute of Optics, Fine Mechanics and Physics, Chinese Academy of Sciences. His research interests include image processing and circuit design in space science.

QINGYU MENG was born in 1986. He received the M.S. degree in optical engineering from the Harbin Institute of Technology, Harbin, China, in 2012. Since 2012, he has been an Assistant Professor with the Changchun Institute of Optics, Fine Mechanics and Physics, Chinese Academy of Sciences. His research interests include optical system design theory and method, optical remote sensing, and advanced optical instrument.